RESEARCH ARTICLE

Influence of Permanent Magnetic Properties on Laser-Assisted Heating Magnetization for Magnetic MEMS

KEITA NAGAI [1], **NAOHIRO SUGITA** [2], **AND TADAHIKO SHINSHI** [2], **(Member, IEEE)**

[1]Department of Mechanical Engineering, Tokyo Institute of Technology, Midori-ku, Yokohama 226-8503, Japan
[2]Laboratory for Future Interdisciplinary Research of Science and Technology (FIRST), Institute of Innovative Research (IIR), Tokyo Institute of Technology, Midori-ku, Yokohama 226-8503, Japan

Corresponding author: Tadahiko Shinshi (shinshi.t.ab@m.titech.ac.jp)

ABSTRACT When magnetic microelectromechanical systems (MEMS) devices utilize thin- or thick-film permanent magnets, the uniform magnetization of these magnets, owing to their flat-shape, generate a strong antimagnetic field and weak surface magnetic flux density. This study proposes a laser-assisted micro multi-pole magnetization method that reduces the antimagnetic field and generates a high surface magnetic flux density. The proposed method involves locally reducing the coercivity through laser-assisted heating and an external reverse magnetic field to selectively reverse the magnetization in heated areas, thereby generating fine and different magnetic patterns on permanent magnets. This study experimentally investigates the relationship between the magnetic properties of twelve NdFeB magnet samples (residual flux density (B_r):1.20-1.39 T and intrinsic coercivity (H_{cj}):955-2388 kA/m) magnetized using the proposed method and the resulting surface magnetic flux densities. Here, the magnetization ratio is introduced as the ratio of the measured to the analyzed surface magnetic flux density. The experimental results reveal that the magnetization ratio increases with an increase in H_{cj}. The highest achieved surface magnetic flux density was 391 mTp-p with a B_r of 1.3 T and H_{cj} of 2388 kA/m. The magnetization ratio was 78.5%. Hence, a higher H_{cj} suppressed the demagnetization. The magnetization ratio peaks around B_r =1.29 T. A higher B_r promotes magnetization reversal, thereby making demagnetization easier. To increase the magnetization ratio and surface magnetic flux density, a permanent magnet with the highest possible H_{cj} and optimal B_r for the magnetization state must be selected. This study has great potential for the development of magnetic MEMS devices.

INDEX TERMS Magnetic MEMS, micro magnetization, multi-pole magnetization, laser-assisted heating, NdFeB magnet.

I. INTRODUCTION

With the recent development of the Internet of Things (IoT), there has been active research and development (R&D) to realize sensors, actuators, and energy harvesters using magnetic MEMS devices [1], [2], [3], [4], [5], [6]. Magnetic MEMS devices utilize the interaction between permanent magnets and coils, permanent magnets, or electromagnets

and the magnetic core [7]. Unlike electrostatic and piezo-electric MEMS devices, a battery can drive magnetic MEMS devices at low voltages without a booster circuit. Different magnetic MEMS devices with permanent magnets several to several hundred micrometers in thickness and less than 10 mm in length [8], [9], [10], [11], [12], [13], [14], [15], [16] have been proposed.

Magnetic MEMS devices use thin-plate magnets machined from sintered NdFeB magnets, thin-film magnets deposited using sputtering, or thick-film magnets deposited using
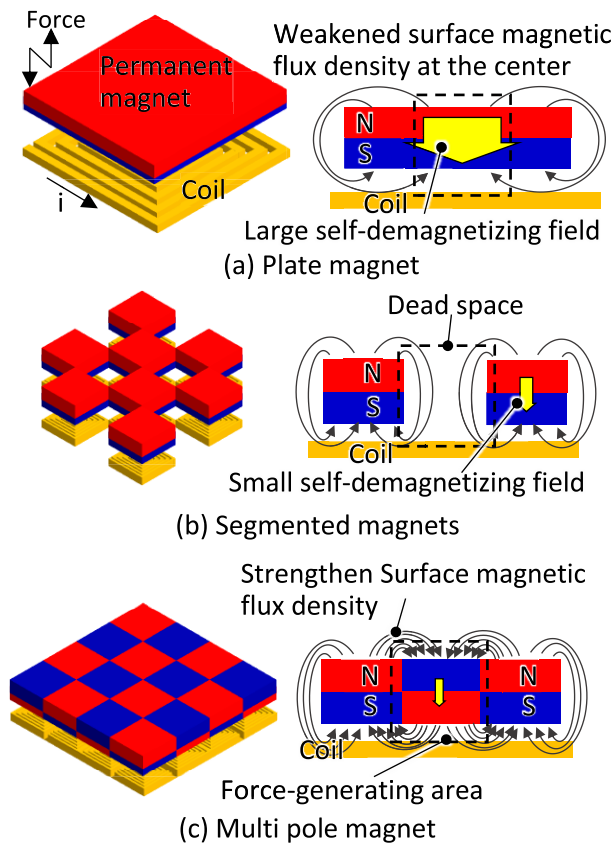
Force
Permanent magnet
Coil
i
Weakened surface magnetic flux density at the center
N
S
Coil
Large self-demagnetizing field
(a) Plate magnet

Dead space
N
S
Coil
Small self-demagnetizing field
(b) Segmented magnets

Strengthen Surface magnetic flux density
N   N
S   S
Coil
Force-generating area
(c) Multi pole magnet

FIGURE 1. Effects of self-demagnetization field to surface magnetic flux density.

pulsed laser deposition. However, a large self-demagnetizing field is generated in the center when a flat-shaped permanent magnet is magnetized in one thickness direction, as shown in Fig. 1(a). The magnetic flux generated from the center of the magnet was small. Magnetic forces cannot be efficiently generated based on the volume of the permanent magnet [17]. To generate a large magnetic flux from the surface of a permanent magnet, the thickness and width of the magnet part forming one pole must be equal. In the case of flat-shaped magnets, slitting to form segments or alternating multi-pole magnetization with a pitch equivalent to their thickness has been proposed.

In previous research, dicing [8], ion milling [9], and wet etching [10] were used to process slits in thin-plate or thick-film magnets such that the width of one pole was almost equal to its thickness. Bonded magnets [11], [12] were used to form the stripe-shaped magnets. Furthermore, segmented magnets are fabricated by electrolytic plating [13], electroless co-deposition [14], and atomic layer deposition [15], as shown in Fig. 1(b).

Alternating multi-pole magnetization without slits in a magnet to effectively generate magnetic flux from one plate or film magnet is also being researched, as shown in Fig. 1(c). One micro alternating multi-pole magnetization method uses pulse current through microcoils [16], [18]. This method

applies a large pulse current of 3–5 kA to the microcoil to generate a magnetic flux density of a few Teslas for magnetization. To magnetize a small width, it is essential to miniaturize the microcoil, although supplying a large current to the microcoil causes it to burn out owing to Joule heat. Consequently, miniaturization has its limits.

There has also been research on the micromagnetization of thin-film magnets using a large-diameter pulsed laser and metal mask [19]. The magnets, wherein the laser beam penetrates the mask, are collectively heated, and an external magnetic field magnetizes the area with reduced coercivity using heat. However, micromagnetization is not easy when magnetizing magnets with a thickness of several hundred micrometers. The external magnetic field also magnetizes the area wherein a laser beam is not irradiated owing to the heat conduction from the laser-heated area.

In this study, we proposed laser-assisted heating [20] to realize the micro multi-pole magnetization of thin-plates and thick-film magnets. In this magnetization method, a laser locally heats the surface of a magnetized magnet in one direction to reduce the coercivity, and an external magnetic field reverses the magnetization direction.

We used slit processing to solve the heat conduction problem that occurs during the micromagnetization of a magnet several hundred micrometers thick. We have achieved alternating stripe patterns with an aspect ratio of 1 [21] and checkerboard-shaped alternating magnetization with an aspect ratio of 0.5 [22] on wire EDM-machined sintered NdFeB magnets with a thickness of 0.5 mm. These magnets had a slit width of 0.15 mm fabricated by dicing.

However, slit processing complicates the magnetization process and possibly breaks the magnets. Hence, we propose a double-sided laser-assisted micro multi-pole magnetization method without slit processing. Here, a short heating time is required to suppress the heat conduction to the adjacent magnetic poles in the without-slit method. Nevertheless, the deeper parts of the magnet cannot be sufficiently heated by short laser heating. The coercivity cannot be lowered enough to cause magnetization reversal. Laser heating on both sides of the magnet for a short time prevents heat conduction to the adjacent magnetic poles, thereby achieving sufficient heating in the deeper parts. By using this method, we achieved the alternating magnetization of 80 poles on a ring magnet with an outer diameter, inner diameter, and thickness of 9.6, 7, and 0.3 mm, respectively, thereby resulting in a maximum surface magnetic flux density of 470 mT [23].

Accordingly, laser-assisted micro multi-pole magnetization can more efficiently generate surface magnetic flux density than segmented magnets. Furthermore, different micromagnetic patterns can be formed for sub-mm-thick magnets by eliminating the slit process.

In this magnetization method, the laser power, scanning path, speed, and spot diameter were experimentally investigated to increase the surface magnetic flux density. However, the measured values were only 75% of the designed values. The designed surface magnetic flux density was
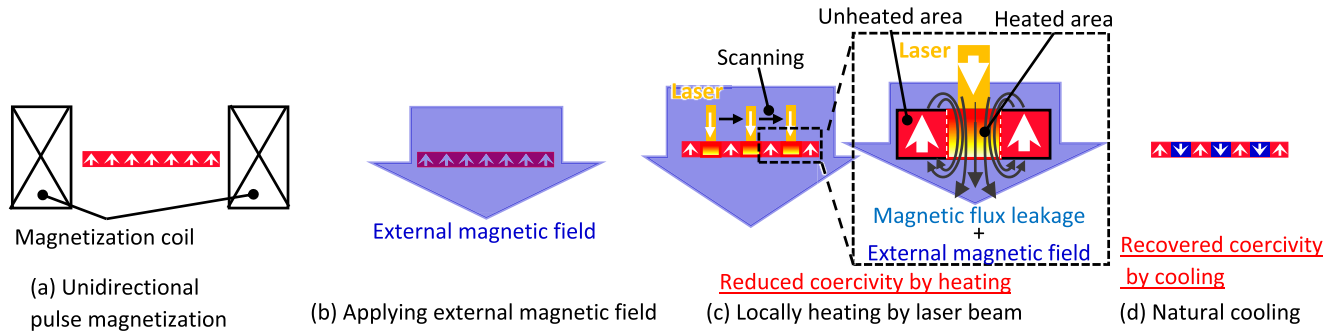
FIGURE 2. Principle of the laser-assisted heating micro multi-pole magnetization method.
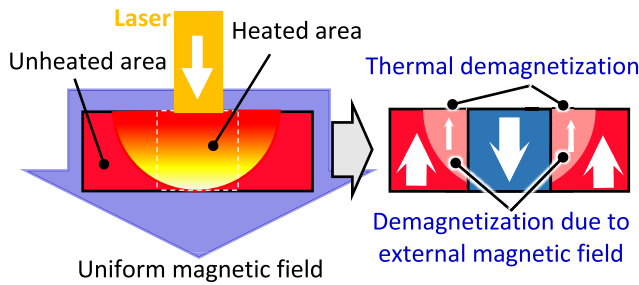

FIGURE 3. Thermal demagnetization in the unheated area owing to external magnetic field.

not achieved because irreversible demagnetization occurred in the unheated areas, wherein the magnetization reversal was not intended, as explained in more details later. The magnetization results of laser-assisted heating are related to the magnetic properties of permanent magnets, but only the influence of the intrinsic coercivity has been clarified [24].

In this research, we aim to develop a laser-assisted heating micro multi-pole magnetization method particularly for magnetic MEMS devices. Further, the study aims to present the relationship between the intrinsic coercivity, residual flux density, and magnetization of the permanent magnets.

From the introduction, Section II elaborates on the laser-assisted micro multi-pole magnetization principle and examines the influence of the magnetic properties and magnetization conditions. Section III describes the experimental methods, conditions, and sample magnets. Section IV discusses the influence of the magnetic properties on laser-assisted fine multi-pole magnetization based on the magnetization results. Section V gives a conclusion of the study.

II. LASER-ASSISTED HEATING MICRO MULTI-POLE MAGNETIZATION METHOD

A. MAGNETIZATION PRINCIPLES AND PHENOMENA

Fig. 2 shows the principle of the laser-assisted heating multipole magnetization method. First, (a) the magnet is magnetized in one direction by applying a pulsed current to the coil. (b) An external magnetic field is applied to the magnet in

the direction opposite to its magnetization. (c) The coercivity is lowered only in the heated area by locally heating the magnet surface using laser scanning. During this process, magnetization reversal along the direction of the external magnetic field occurs in the heated area. Additionally, the flux leakage from the adjacent poles flows in a direction that promotes magnetization reversal in the heated area. (d) Natural cooling then recovers coercivity, and magnetization reversal finishes. Different micro- and magnetic patterns can be formed by repeating these processes.

The external magnetic field must be sufficiently large relative to the coercivity of the magnet sample, which decreases owing to laser heating, to reverse the magnetization in this method. Furthermore, as shown in Fig. 3, two other unintended phenomena occur in adjacent magnetic poles simultaneously: 1) irreversible demagnetization owing to the uniform external magnetic field used for magnetization reversal, and 2) thermal demagnetization owing to the thermal conduction. For this reason, magnetization reversal in the heated area and demagnetization owing to the heat and demagnetization field in the unheated area must be considered. The next section discusses the relationship between the magnetization phenomena in the heated and unheated areas and the residual flux density B_r, intrinsic coercivity H_{cj}, and temperature of the permanent magnet.

B. INFLUENCE OF MAGNETIZATION CONDITIONS

Fig. 4(a) shows the relationship between the heating temperature T, coercivity H_c of the magnet, and external magnetic field H_{Ext} used for magnetization reversal. Here, H_c decreases as T increases and becomes zero above the Curie temperature T_C. The magnetization reversal begins when H_c is lower than H_{Ext}. As H_{Ext} increased, the magnetization reversal starting temperature T_{rev} decreased ($T_{rev1} \rightarrow T_{rev2}$).

Fig. 4(b) shows the relationship between the temperature T_{LH} and residual flux density B_{rLH} of the heated area. The solid line shows the B_{rLH}, wherein demagnetization progresses as T_{LH} increases. The magnetization reverses beyond T_{rev}, and B_{rLH} gradually increases, thus reaching saturation at T_{sat}. When T_{LH} exceeds T_{demag}, irreversible thermal demagnetization begins. Finally, the heated area demagnetizes at T_{degau}, and B_{rLH} becomes zero. As the
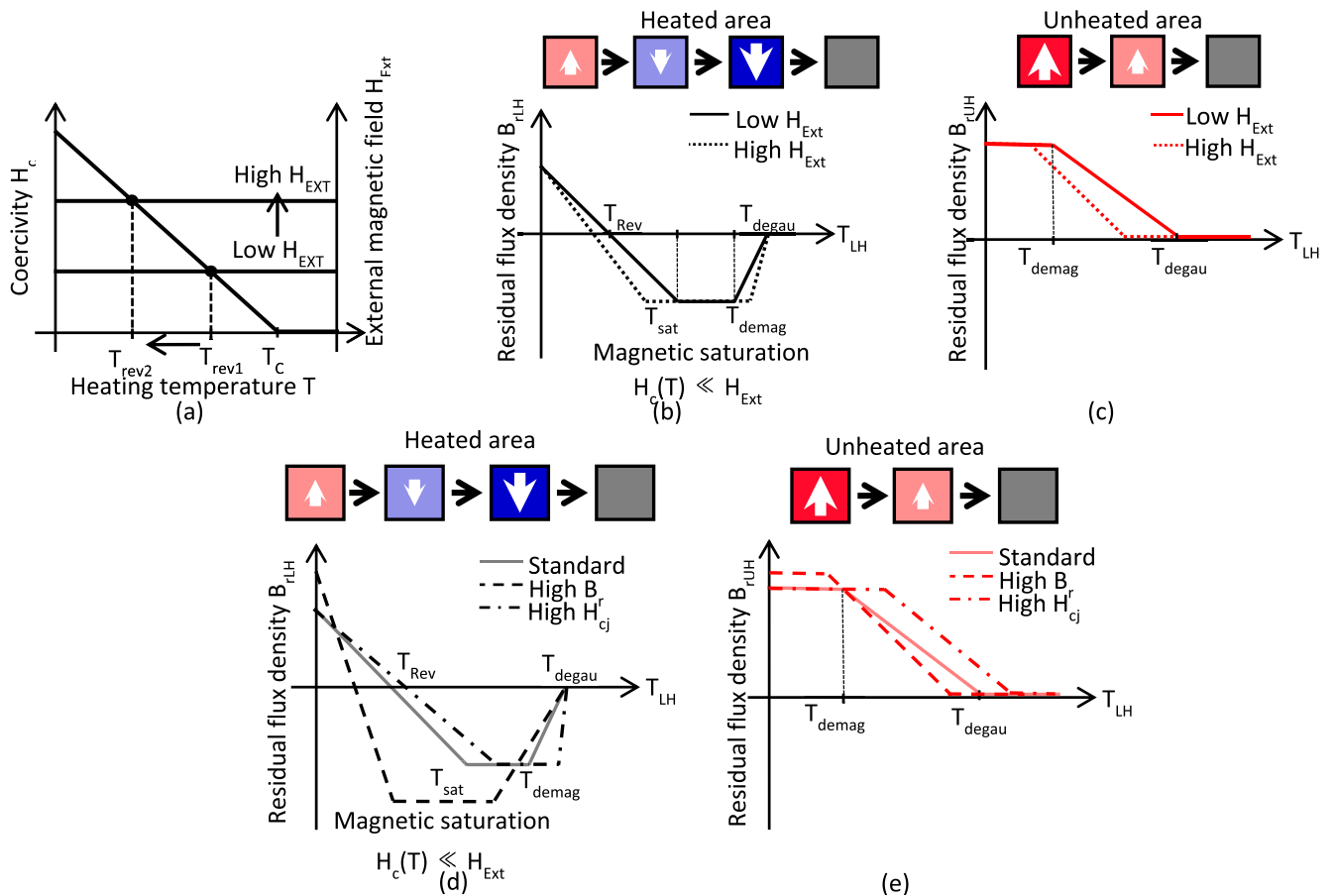
FIGURE 4. Relationship between residual flux density in each region, external magnetic field, heating conditions, and permanent magnet properties, (a) relationship between the heating temperature, coercivity, and external magnetic field, (b) relationship between the temperature and residual flux density of the heated area, (c) relationship between the heating temperature and residual flux density of the unheated area, (d) variation of the residual flux density with the temperature for magnet materials with a high B_r and H_{cj}, and (e) Variation of the residual flux density with the temperature for a high B_r and H_{cj}.

external magnetic field increases, as represented by the dotted line, T_{sat} at which magnetic saturation occurs decreases, although T_{demag} increases.

Fig. 4(c) shows the relationship between the heating temperature T_{UH} and residual flux density B_{rUH} of the unheated area. T_{UH} increases owing to the heat conduction from the heated area. B_{rUH}, as represented by the solid line, decreases owing to the irreversible demagnetization starting at T_{demag}. Finally, the unheated area demagnetizes at T_{degau} or above, and B_{rUH} becomes zero. The dotted line shows that T_{demag} and T_{degau} decreased as the external magnetic field increased.

C. INFLUENCE OF MAGNETIC PROPERTIES

The dashed and single-pointed lines in Fig. 4(d) show the variation in B_{rLH} with the temperature for magnet materials with high a B_r and H_{cj}, respectively. For a similar H_{cj}, the higher the B_r, the lower the H_c, T_{rev}, and T_{sat} because more flux leakage from adjacent magnetic poles is given to the heated area. B_{rLH} increases when magnetic saturation occurs,

thus resulting in a decrease in T_{demag}. A higher H_{cj} also has a higher T_{rev}, T_{sat}, and T_{demag}.

The dashed and single-pointed lines in Fig. 4(e) show the variation in B_{rUH} with the temperature for high B_r and H_{cj}, respectively. When B_r was high, T_{demag} and T_{degau} decreased. As H_{cj} increased, T_{demag} and T_{degau} increased.

As described earlier, the enhancement of the magnetization reversal in the heated area requires a higher external magnetic field, heating temperature, and B_r. However, suppressing the irreversible demagnetization in the unheated area requires a lower external magnetic field, lower heating temperature, and higher H_{cj}. Based on this basic principle, a survey is carried out for magnet materials suitable for laser-assisted heating micro multi-pole magnetization.

III. EXPERIMENTAL METHODS
A. EXPERIMENTAL SETUP AND PROCESS
The magnet samples were unidirectionally magnetized using a pulse magnetizer (CM-2510-30S, Denshi Magneto Kogyo). Laser scanning was performed on the magnet samples using a laser marking device (YVO$_4$ laser, wavelength 532 nm

MD-S9910, Keyence). The experimental environment was at 22°C of room temperature in the atmosphere. For each magnet sample, the magnetization conditions that maximize the surface magnetic flux density are determined by changing the laser scanning speed and external magnetic field strength, as presented in Table 1. The magnet samples were multi-pole magnetized under the surveyed conditions, and the surface magnetic flux density was measured.

TABLE 1. Magnetization conditions.

Laser type	Repetition freq. [kHz]	Spot dia. [mm]	Scan pitch [mm]	Laser power [W]	Scan speed [mm/s]	External mag. field [T]
YVO$_4$ 532 nm	30	0.1	0.6	6	130 - 200	0.3 – 0.7

Fig. 5 shows the surface magnetic flux density measurement system. The magnetic flux density above 100 μm of the magnet surface was measured by tracing the magnet using a Hall element (Asahi Kasei Electronics, HG-0711) with a 50 μm square magnet-sensitive area at the tip of the probe. For each magnet sample, the measured surface magnetic flux density ratio to the simulated one, that is, the magnetization ratio, was evaluated.
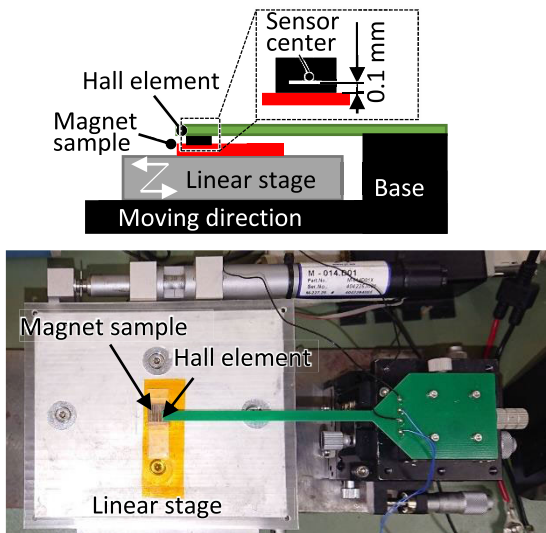

FIGURE 5. Surface magnetic flux density measurement system.

B. MAGNET SAMPLES

Twelve types of NdFeB magnet samples with different magnetic properties were used. Table 2 presents the (BH)$_{max}$, residual flux density B$_r$, intrinsic coercivity H$_{cj}$, and heat-resistance temperature of the samples. There is no international standard for the heat resistance temperature. Hence [25], the temperature at which the irreversible thermal demagnetization begins in a magnet sample with a specific shape defined by a company and released as catalog data is used. Magnet samples were machined by wire EDM to

TABLE 2. Magnetic properties of NdFeB magnet samples.

Test sample	(BH)$_{max}$ [kJ/m^3]	Residual flux density B$_r$ [T]	Intrinsic coercivity H$_{cj}$ [kA/m]	Working temp. [°C]
No. 1	279	1.20	955	90
No. 2	318	1.28	955	85
No. 3	358	1.35	955	85
No. 4	279	1.20	1353	130
No. 5	318	1.28	1353	120
No. 6	382	1.39	1353	120
No. 7	279	1.20	1592	160
No. 8	318	1.28	1592	150
No. 9	358	1.35	1592	150
No. 10	358	1.33	2000	180
No. 11	302	1.24	2388	200
No. 12	334	1.30	2388	200

5 × 5×t0.3 mm from a sintered bulk NdFeB magnet with each magnetic property.

C. SEARCH FOR MAGNETIZATION CONDITIONS THAT GENERATE MAXIMUM SURFACE MAGNETIC FLUX DENSITY

Under the magnetization conditions presented in Table 1, the laser scanning speed and magnitude of the external magnetic field that maximize the surface magnetic flux density are determined for each magnet sample. The magnet surface is divided to increase the efficiency of the search for magnetization conditions. The target magnetization width and sample size determine the number of divisions. In addition, to minimize the influence of edge effects, each region should have an area that can magnetize about seven poles. As shown in Fig. 6, the magnet surface was divided into eight regions. The laser scanning speed was varied in each region, and seven poles were alternately magnetized with a magnetization width of 0.3 mm. Although there may be an optimal sequence of laser irradiation depending on the magnetization pattern and magnet shape, in this experiment, we irradiated the magnets in order, starting from the left end of the magnet. In Fig. 6, the first column on the left side of regions (1), (3), (5), and (7) is heated in a straight line at different speeds. After the magnet has cooled completely, the next column to the right, located 0.6 mm away, is heated. The spacing between the fourth and fifth irradiation lines across the even-numbered region from the odd-numbered region is 1.2 mm. This process was repeated until four lines were irradiated in each region.

An external magnetic field was generated in the direction of the thickness of each magnet sample, as shown in Fig. 7. The magnitude of the external magnetic field was changed by combining several sintered NdFeB magnets (magnet base material: N35, MagFine Corp.). Three types of magnets or magnet arrays with different magnet dimensions, numbers, and arrangements are prepared to generate external magnetic

fields of 0.3, 0.5, and 0.7T. Table 3 summarizes the magnet dimensions for external magnetic fields of 0.3 and 0.5 T.
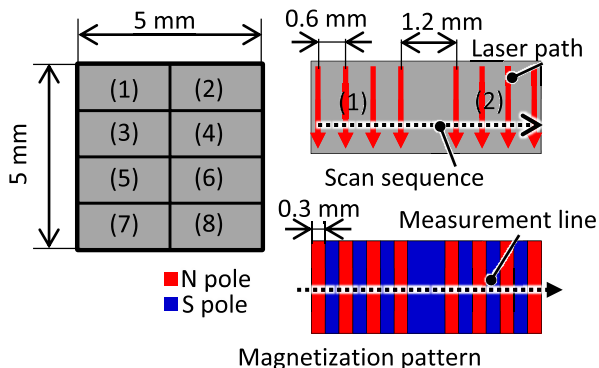

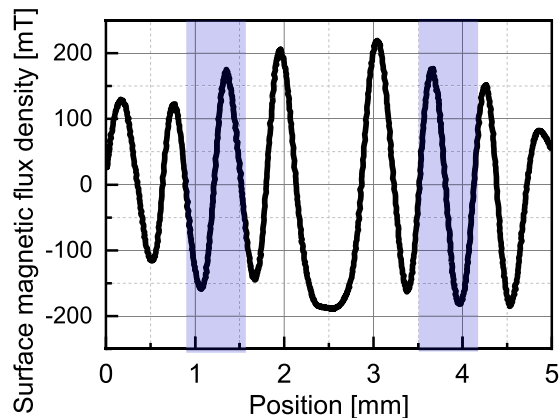FIGURE 6. Magnet surface regions and laser scanning sequence for magnetization condition search.
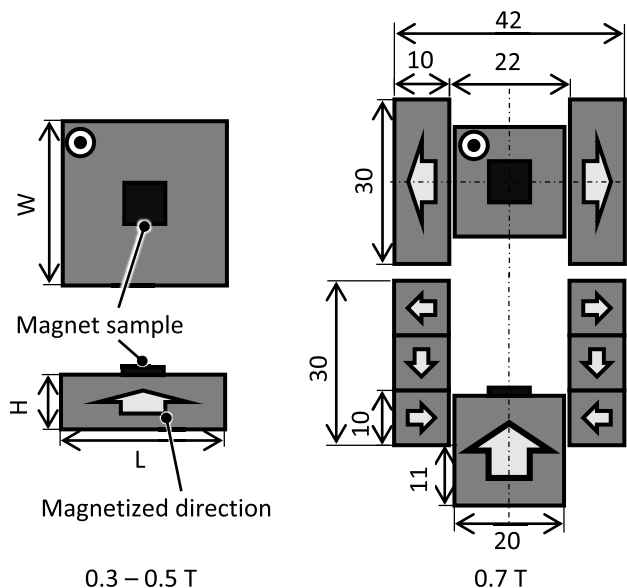

FIGURE 7. External magnetic field application method.

TABLE 3. Dimensions of magnets used for applying external magnetic field.

External mag. field [T]	Length L [mm]	Width W [mm]	Hight H [mm]
0.3	30	30	10
0.5	20	20	20

The surface magnetic flux density on the centerline of each magnet region that has been multi-pole magnetized under different magnetization conditions was measured. Fig. 8 shows the measured surface magnetic flux density in the region of No. 5 magnetized at a laser scanning speed of 150-160 mm/s with an external magnetic field of 0.3 T. Two surface magnetic flux density distribution regions can

FIGURE 8. Example of measurement results of surface magnetic flux density distribution with the magnetization condition (No. 5, 150–160 mm/s, and 0.3 T).

be measured on a single line. The laser scanning speed and external magnetic field that maximizes the surface magnetic flux density p-p values of a single pole pair with small edge effects near the center of each region with small edge effects in the range of 0.9 to 1.5 mm and 3.5 to 4.1 mm, respectively, are determined.
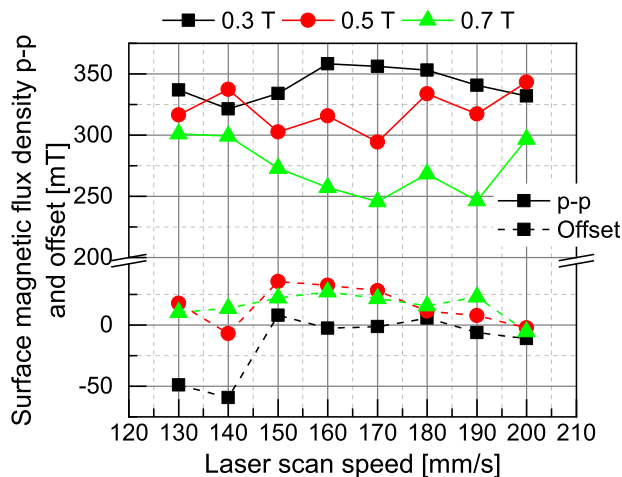

FIGURE 9. Surface magnetic flux density for each magnetization condition for No. 5.

For example, Fig. 9 shows the relationship between the laser scanning speed and p-p and offset values of the surface magnetic flux density of the No. 5 sample when different external magnetic fields are applied. The closer the offset is to zero, the more ideal alternating magnetization is achieved. The zero offsets reveal that positive and negative magnetizations are achieved equally. The maximum peak-to-peak value of the surface magnetic flux density of No. 5 occurs when the laser scanning speed and external magnetic field are 160 mm/s and 0.3 T, respectively, and while the offset approaches zero.

D. EVALUATION OF INFLUENCE OF MAGNETIC PROPERTIES

As shown in Fig. 10, a new magnet sample is alternately magnetized in stripes with a width of 0.3 mm and 16 poles under the determined conditions to evaluate the influence of the magnetic properties on magnetization. The laser scanning sequence started sequentially from the left side of the magnet. This is because in the magnetization condition search as shown in Fig. 8, nonuniform alternating magnetization is formed on the entire magnet sample owing to the different scanning speeds in each region and area that is wider than the magnetization width in the center of the magnet sample.
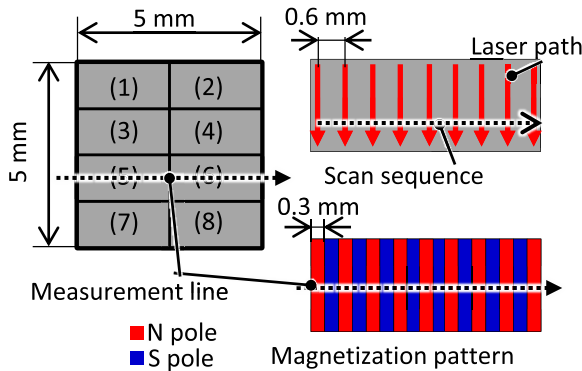
FIGURE 10. Alternating magnetization using the searched magnetization conditions.

The influence of magnetic properties is evaluated using the magnetization ratio *MagR* defined in Equation (1) as the average measured p-p surface magnetic flux density $B_{Meas\ p-p}$ of the eight poles with small edge effects in the range of 1.5 to 3.5 mm to the simulated one $B_{Sim\ p-p}$, as shown in Fig. 11.

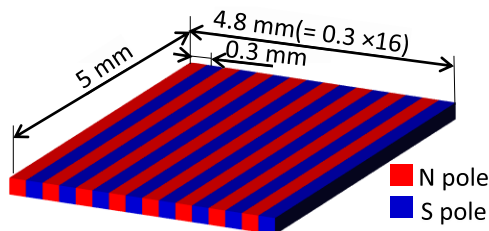$$MagR = \frac{B_{Meas\ p-p}}{B_{sim\ p-p}} \times 100 \qquad (1)$$

FIGURE 11. Simulation model to obtain the design value of the surface magnetic flux density.

In the three-dimensional magnetic field analysis (Ansys Electronics Desktop 2021 R1, ANSYS Inc.), the catalog values of the magnetic properties of each magnet were used. Fig. 12 compares the simulated and measured magnetic flux density distribution of No. 5 sample.
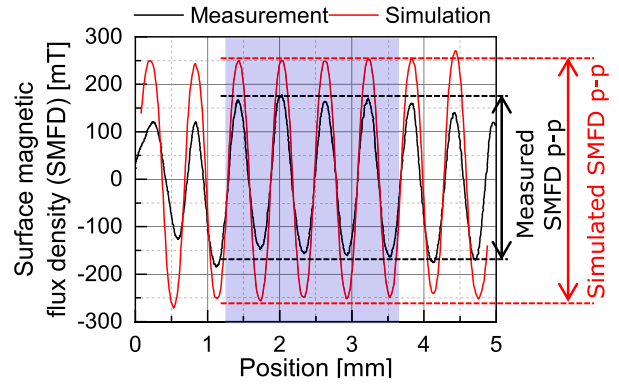

FIGURE 12. Surface magnetic flux density distribution with alternating magnetization (No.5, 140 mm/s, 0.3 T).

TABLE 4. Magnetization conditions that generate maximum surface magnetic flux density experimentally searched for each magnet.

Magnet type	Scan speed [mm/s]	Ext. mag. Field [mm]
No. 1	170	0.3
No. 2	180	0.3
No. 3	190	0.3
No. 4	180	0.3
No. 5	140	0.3
No. 6	200	0.3
No. 7	180	0.3
No. 8	160	0.3
No. 9	180	0.3
No. 10	200	0.5
No. 11	160	0.5
No. 12	200	0.5

## IV. EXPERIMENTAL RESULTS AND DISCUSSION

A. RELATIONSHIP BETWEEN MAGNETIC PROPERTIES AND SURFACE MAGNETIC FLUX DENSITY

The magnetization conditions under which the maximum surface magnetic flux density p-p values were obtained for each magnetic sample are summarized in Table 4. Fig. 13 shows the relationship between B_r, H_{cj}, and the surface magnetic flux density p-p values after magnetization. Fig. 13(a) shows that the surface magnetic flux density increased as H_{cj} increased, although the slope of the increase decreased after 1500 kA/m. The highest H_{cj} sample generates the highest surface magnetic flux density p-p of 391 mT.
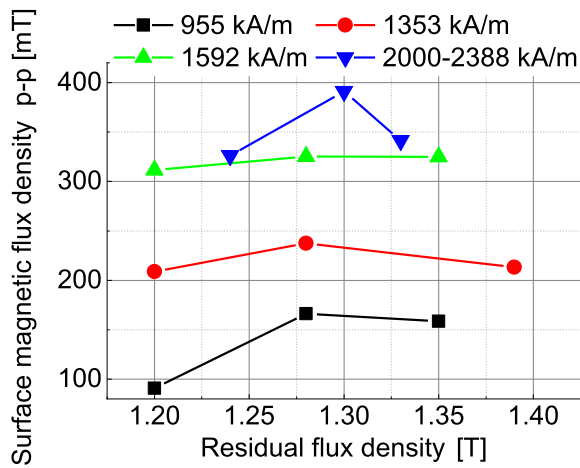
In Fig. 13(b), the surface magnetic flux density peaks around B_r of 1.29 T for a group of magnet samples with similar H_{cj}. Excluding samples with an H_{cj} of 2000 kA/m or higher, the changes become smaller as H_{cj} increases. The surface magnetic flux density distribution of No. 12, which had the highest H_{cj} and surface magnetic flux density p-p, is shown in Fig. 14.

B. RELATIONSHIP BETWEEN MAGNETIC PROPERTIES AND MAGNETIZATION RATIO

Fig. 15 shows the relationship between B_r, H_{cj}, and the magnetization ratio. Fig. 15(a) shows that the magnetization
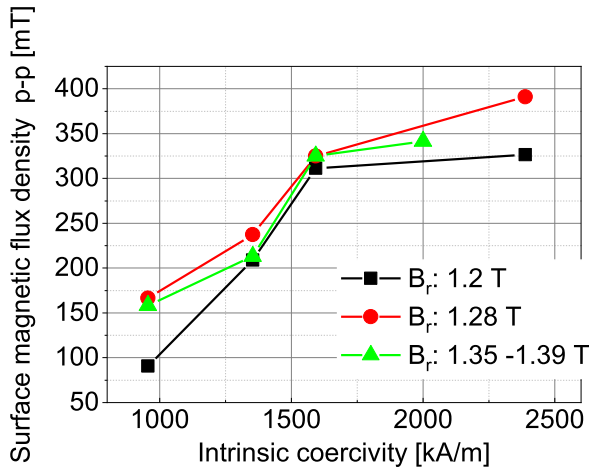
FIGURE 13. Relationship between each magnetic property and the surface magnetic flux density: (a) Relationship between the intrinsic coercivity and surface magnetic flux density and (b) relationship between residual flux density and surface magnetic flux density.
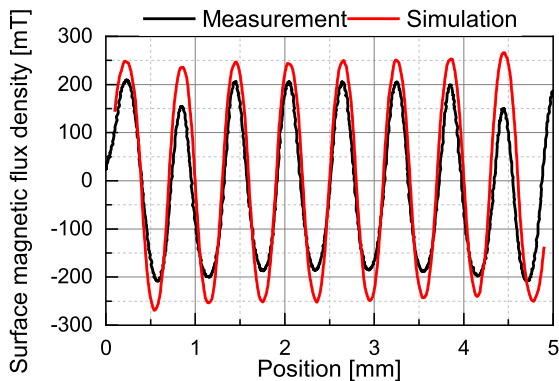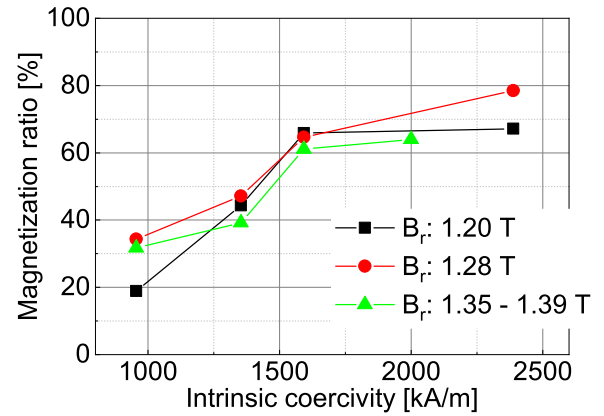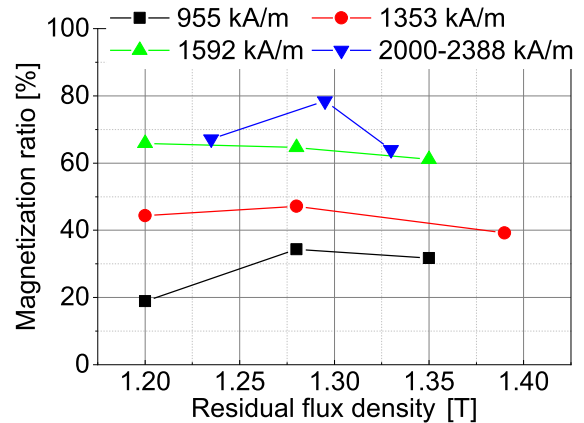

FIGURE 14. Magnetization results for No. 12 with the highest surface magnetic flux density.

ratio increased when H_{cj} increased. The slope becomes smaller when H_{cj} exceeds 1592 kA/m, and the magnetization ratio of the samples with 1.2 and 1.35–1.39 T changes by only 2%.

FIGURE 15. Relationship between each magnetic property and the magnetization ratio: (a) Relationship between intrinsic coercivity and magnetization ratio, and (b) relationship between residual flux density and magnetization ratio.

The No. 12 sample has the highest magnetization ratio of 78.5%. In Fig. 15 (b), the magnetization ratio peaks between 1.25–1.3 T. The difference in the magnetization ratio decreased as H_{cj} increased for samples with an H_{cj} of 1592 kA/m or lower.

C. DISCUSSION

This section discusses the causes of the increase in the surface flux density and magnetization ratio with a higher H_{cj} and peaks around a particular B_r. As described in Chapter 2, the laser-assisted micro multi-pole magnetization method causes magnetization reversal, thermal demagnetization, and demagnetization owing to the external and leakage fields. The two demagnetization phenomena are described below.

Fig. 16 shows the changes in the knick and operating points owing to heating or an external magnetic field. The thermal demagnetization and demagnetization owing to the demagnetization field are related to the magnetic flux density of the knick point B_k, which is a bending point on the demagnetization curve, and the magnetic flux density of the operating point B_o, which is the intersection of the permeance

line and demagnetization curve mainly determined by the magnet shape in this study.

From Fig. 16, B_k increases as the heating temperature increased. When B_k exceeds B_o, demagnetization occurs, and the difference represents the magnitude of the demagnetization. Here, B_o decreases when an external magnetic field is applied, and demagnetization occurs when B_o is less than B_k, as in thermal demagnetization. Furthermore, magnetization reversal occurs instead of demagnetization when a sufficient external magnetic field is applied.
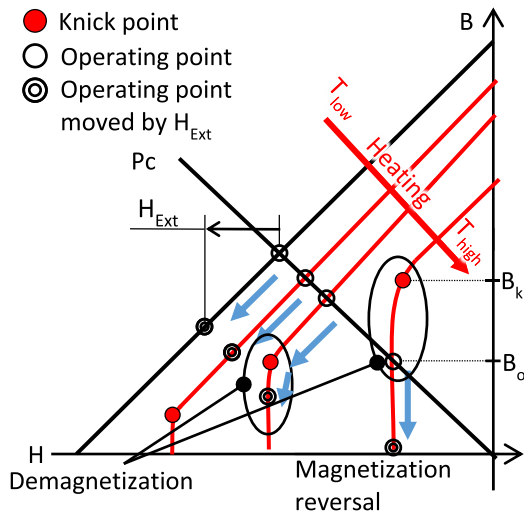

FIGURE 16. Variation in the knick and operating points when the heating temperature is varied and an external magnetic field is applied on the demagnetization curve.

The relationship between the knick points and magnetic properties is shown in Fig. 17. Fig. 17(a) shows the demagnetization curves for the different values of H_{cj}. The blue and red lines represent the J-H and B-H curves, respectively. The solid and dashed lines represent the difference in H_{cj}, with the dashed line representing a larger H_{cj}. When H_{cj} is small, a knick point appears at the heating temperature T_1, and demagnetization occurs at T_2. However, when H_{cj} was high, the knick point began to appear at T_2, and demagnetization did not occur until the temperature was higher. Fig. 17(b) shows the demagnetization curves for different B_r. The solid and dashed lines denote the difference in B_r, with B_r being larger in the dashed line. When B_r is small, demagnetization occurs at T_2. However, when B_r is high, demagnetization occurs at T_1, and a larger demagnetization occurs at T_2. Hence, the irreversible demagnetization increases as the heating temperature increases, the applied reverse magnetic field is strengthened, or B_r increases. However, it can be suppressed if H_{cj} is high.

This is the reason for the increased surface magnetic flux density and magnetization ratio with a higher H_{cj}. Here, thermal demagnetization occurs in the heated and unheated areas owing to the temperature rise by thermal conduction, although it is suppressed when H_{cj} is high. Furthermore, in the unheated area, irreversible demagnetization occurs as
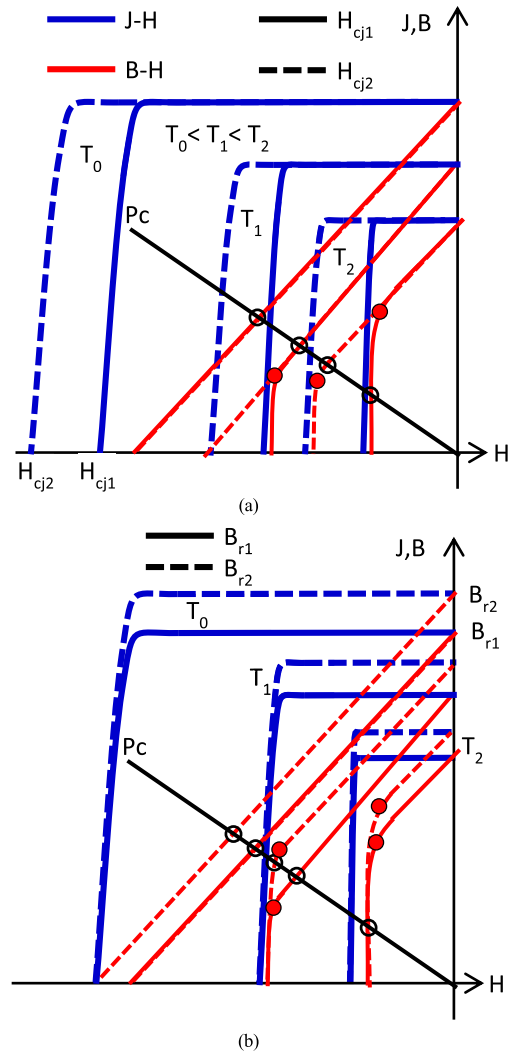

(a)

(b)

FIGURE 17. Variation of knick points on demagnetization curves with different magnetic properties. (a) Different intrinsic coercivities H_{cj} (b) Different residual magnetic flux densities B_r.

the external magnetic field applied for magnetization reversal becomes a demagnetization field. However, it is suppressed in the exact mechanism of the thermal demagnetization when H_{cj} is high. Hence, the surface magnetic flux density after magnetization and magnetization ratio increases when H_{cj} is high.

The following explains why the surface magnetic flux density and magnetization ratio peak at approximately 1.29 T for a group of magnet samples with a similar H_{cj}. When B_r is small, the flux leakage from the adjacent unheated area in the heated area becomes small. Consequently, sufficient magnetization reversal does not occur in the heated area. Additionally, when B_r is large, magnetization reversal occurs in the heated area. However, because the knick point appears at low temperatures, this results in strong thermal demagnetization of the entire magnet and that owing to the external magnetic field in the unheated area. The peak appears at a specific B_r for each group of magnetic materials with different H_{cj}. The difference in the magnetization results

with similar H_{cj} became smaller as H_{cj} increased, except for materials with an H_{cj} of 2000 kA/m or higher because the B_r was not aligned with those of the other groups of samples. This is because the two demagnetizations of the magnet are suppressed as H_{cj} increases.

These discussions show that to obtain a high surface magnetic flux density and magnetization ratio in laser-assisted magnetization, a magnetic material with a high H_{cj} and B_r must be selected. Further, B_r must not only be high, but the knick and operating point from the magnetization shape must also be considered to minimize irreversible demagnetization.

V. CONCLUSION

This study investigated the effects of the residual flux density B_r and intrinsic coercivity H_{cj} of the NdFeB magnets on the surface flux density and magnetization ratio after micro-multipole magnetization using laser-assisted heating. Twelve NdFeB magnet samples were used in the experiments. The magnet sample with B_r of 1.29 T and H_{cj} of 2388 kA/m had the highest surface magnetic flux density of 391 mT and magnetization ratio of 78.5%. The surface magnetic flux density and magnetization ratio increased when H_{cj} increased.

A higher intrinsic coercivity effectively mitigates two types of demagnetization: thermal demagnetization of the magnet and demagnetization resulting from an external magnetic field that results in a demagnetization field in the unheated area. Furthermore, for a group of magnet samples with a similar H_{cj}, the surface magnetic flux density and magnetization ratio were highest when B_r was approximately 1.29 T. This is because the flux leakage generated from the unheated area is applied to the heated area, wherein magnetization reversal occurs, and is enhanced as B_r increases. Conversely, as B_r decreases, the magnetization reversal is insufficient. However, increasing B_r excessively results in a higher magnetization ratio to the two types of demagnetization owing to a lower knick point appearing temperature. Hence, to obtain a high surface magnetic flux density and magnetization ratio, it is necessary to select a magnet material with an H_{cj} as high as possible and with a suitable B_r based on the magnetization pattern that defines the knick point to reduce irreversible demagnetization.

We will collect data on magnetization reversal and demagnetizations by heating and cooling the magnet while applying a magnetic field. Based on these data, we will construct a mathematical model in the future. To further improve the surface magnetic flux density and magnetization ratio, the magnetic field in the heated area is made stronger, and that in the unheated area is made weaker. As a result, magnetization reversal in the heated area is promoted, and demagnetization in the unheated area is suppressed.

REFERENCES

[1] Y. Tan, Y. Dong, and X. Wang, "Review of MEMS electromagnetic vibration energy harvester," *J. Microelectromech. Syst.*, vol. 26, no. 1, pp. 1–16, Feb. 2017, doi: 10.1109/JMEMS.2016.2611677.

[2] L.-Y. Ma, N. Soin, M. H. M. Daut, and S. F. W. M. Hatta, "Comprehensive study on RF-MEMS switches used for 5G scenario," *IEEE Access*, vol. 7, pp. 107506–107522, 2019, doi: 10.1109/ACCESS.2019.2932800.

[3] E. Martínez-Cisneros, L. A. Velosa-Moncada, E. A. Elvira-Hernández, O. I. Nava-Galindo, L. A. Aguilera-Cortés, R. Pérez-Cuapio, A. de León, F. López-Huerta, R. Salgado-Estrada, and A. L. Herrera-May, "Analytical modeling of the mechanical behavior of MEMS/NEMS-multilayered resonators with variable cross-sections for sensors and energy harvesters," *IEEE Access*, vol. 9, pp. 81040–81056, 2021, doi: 10.1109/ACCESS.2021.3084600.

[4] S. Roy, D. Mallick, and K. Paul, "MEMS-based vibrational energy harvesting and conversion employing micro-/nano-magnetics," *IEEE Trans. Magn.*, vol. 55, no. 7, pp. 1–15, Jul. 2019, doi: 10.1109/TMAG.2019.2896105.

[5] S. N. Nejad and R. Mansour, "Development of MEMS Reed magnetic sensors," *IEEE Trans. Magn.*, vol. 52, no. 2, pp. 1–7, Feb. 2016, doi: 10.1109/TMAG.2015.2484282.

[6] G. Schiavone, A. S. Bunting, M. P. Y. Desmulliez, and A. J. Walton, "Fabrication of electrodeposited Ni–Fe cantilevers for magnetic MEMS switch applications," *J. Microelectromech. Syst.*, vol. 24, no. 4, pp. 870–879, Aug. 2015, doi: 10.1109/JMEMS.2014.2355214.

[7] O. Cugat, J. Delamare, and G. Reyne, "Magnetic micro-actuators and systems (MAGMAS)," *IEEE Trans. Magn.*, vol. 39, no. 6, pp. 3607–3612, Nov. 2003, doi: 10.1109/TMAG.2003.816763.

[8] D. Han, T. Shinshi, N. Azuma, and S. Kadota, "An in-plane, large-stroke, multipole electromagnetic microactuator realized by guideways stacking mechanism," *Sens. Actuators A, Phys.*, vol. 298, Oct. 2019, Art. no. 111563, doi: 10.1016/j.sna.2019.111563.

[9] C. Zhi, T. Shinshi, M. Saito, and K. Kato, "Planar-type micro-electromagnetic actuators using patterned thin film permanent magnets and mesh type coils," *Sens. Actuators A, Phys.*, vol. 220, pp. 365–372, Dec. 2014, doi: 10.1016/j.sna.2014.10.012.

[10] Y. Wang, C. Zhi, B. Tang, K. Yang, J. Xie, W. Xu, H. Li, and X. Wang, "A micro electromagnetic actuator with high force density," *Sens. Actuators A, Phys.*, vol. 331, Nov. 2021, Art. no. 112771, doi: 10.1016/J.SNA.2021.112771.

[11] C. Qi, D. Han, and T. Shinshi, "A MEMS-based electromagnetic membrane actuator utilizing bonded magnets with large displacement," *Sens. Actuators A, Phys.*, vol. 330, Oct. 2021, Art. no. 112834, doi: 10.1016/J.SNA.2021.112834.

[12] K. Tao, J. Wu, A. G. P. Kottapalli, D. Chen, Z. Yang, G. Ding, S. W. Lye, and J. Miao, "Micro-patterning of resin-bonded NdFeB magnet for a fully integrated electromagnetic actuator," *Solid-State Electron.*, vol. 138, pp. 66–72, Dec. 2017, doi: 10.1016/J.SSE.2017.09.006.

[13] M. Han, Q. Yuan, X. Sun, and H. Zhang, "Design and fabrication of integrated magnetic MEMS energy harvester for low frequency applications," *J. Microelectromech. Syst.*, vol. 23, no. 1, pp. 204–212, Feb. 2014, doi: 10.1109/JMEMS.2013.2267773.

[14] S. Guan and B. J. Nelson, "Fabrication of hard magnetic microarrays by electroless codeposition for MEMS actuators," *Sens. Actuators A, Phys.*, vol. 118, no. 2, pp. 307–312, Feb. 2005, doi: 10.1016/j.sna.2004.08.020.

[15] M. T. Bodduluri, B. Gojdka, N. Wolff, L. Kienle, T. Lisec, and F. Lofink, "Investigation of wafer-level fabricated permanent micromagnets for MEMS," *Micromachines*, vol. 13, no. 5, p. 742, May 2022, doi: 10.3390/MI13050742.

[16] R. Fujiwara, T. Shinshi, and M. Uehara, "Positioning characteristics of a MEMS linear motor utilizing a thin film permanent magnet and DLC coating," *Int. J. Autom. Technol.*, vol. 7, no. 2, pp. 148–155, Mar. 2013, doi: 10.20965/IJAT.2013.P0148.

[17] K. Paul, D. Mallick, and S. Roy, "Performance improvement of MEMS electromagnetic vibration energy harvester using optimized patterns of micromagnet arrays," *IEEE Magn. Lett.*, vol. 12, pp. 1–5, 2021, doi: 10.1109/LMAG.2021.3088403.

[18] J. Töpfer, B. Pawlowski, H. Beer, K. Plötner, P. Hofmann, and J. Herrfurth, "Multi-pole magnetization of NdFeB magnets for magnetic micro-actuators and its characterization with a magnetic field mapping device," *J. Magn. Magn. Mater.*, vol. 270, nos. 1–2, pp. 124–129, Mar. 2004, doi: 10.1016/J.JMMM.2003.08.008.

[19] F. Dumas-Bouchiat, L. F. Zanini, M. Kustov, N. M. Dempsey, R. Grechishkin, K. Hasselbach, J. C. Orlianges, C. Champeaux, A. Catherinot, and D. Givord, "Thermomagnetically patterned micromagnets," *Appl. Phys. Lett.*, vol. 96, no. 10, Mar. 2010, doi: 10.1063/1.3341190.

[20] R. Fujiwara, T. Shinshi, and E. Kazawa, "Micromagnetization patterning of sputtered NdFeB/Ta multilayered films utilizing laser assisted heating," *Sens. Actuators A, Phys.*, vol. 220, pp. 298–304, Dec. 2014, doi: 10.1016/J.SNA.2014.10.011.

[21] R. Fujiwara, S. Tanaka, W. Hijikata, and T. Shinshi, "Sub-millimeter pitch multipole magnetization in a sintered Nd-Fe-B magnet utilizing laser heating," *IEEE Magn. Lett.*, vol. 7, pp. 1–4, 2016, doi: 10.1109/LMAG.2015.2508004.

[22] N. Azuma, S. Tanaka, R. Fujiwara, T. Shinshi, and K. Suzuki, "A two-degree-of-freedom micro electromagnetic actuator utilizing a fine pitch and multi-pole magnetized permanent magnet," *J. Jpn. Soc. Precis. Eng.*, vol. 84, no. 3, pp. 289–294, Mar. 2018, doi: 10.2493/JJSPE.84.289.

[23] D. Han, K. Nagai, and T. Shinshi, "High torque micro slice motor using a multipole ring magnet," *Sens. Actuators A, Phys.*, vol. 311, Aug. 2020, Art. no. 112050, doi: 10.1016/j.sna.2020.112050.

[24] K. Nagai, N. Sugita, and T. Shinshi, "Survey of permanent magnet for a laser-assisted heating magnetization to generate designed surface magnetic flux density distribution for magnetic MEMS devices," in *Proc. 21st Int. Conf. Micro Nanotechnol. Power Gener. Energy Convers. Appl. (PowerMEMS)*, Dec. 2022, pp. 232–233, doi: 10.1109/POWER-MEMS56853.2022.10007554.

[25] W. Gao, X. Kang, J. Zhang, and Z. Chi, "Determining the maximum operating temperature of permanent magnets via in-situ measurement of the magnetic flux," *J. Magn. Magn. Mater.*, vol. 562, Nov. 2022, Art. no. 169744, doi: 10.1016/J.JMMM.2022.169744.

NAOHIRO SUGITA received the B.S., M.S., and Ph.D. degrees in mechanical engineering from Keio University, Yokohama, Japan, in 2012, 2014, and 2017, respectively. From 2017 to 2019, he was a Researcher with the Products Development Center, IHI Corporation, Yokohama. Since 2019, he has been an Assistant Professor with the Laboratory for Future Interdisciplinary Research of Science and Technology, Tokyo Institute of Technology. His research interests include mechanical and acoustic resonances, nonlinear vibration, ultrasound cavitation, bubble oscillations in the ultrasound field, and medical ultrasound applications.

KEITA NAGAI was born in Saitama, Japan, in 1995. He received the B.S. degree in science and engineering from Hosei University, Japan, in 2018, and the M.S. degree in mechanical engineering from the Tokyo Institute of Technology, Japan, in 2020, where he is currently pursuing the Ph.D. degree in mechanical engineering. His research interests include magnetic microactuators and micro-magnetization.

TADAHIKO SHINSHI (Member, IEEE) received the B.E., M.E., and D.Eng. degrees from the Tokyo Institute of Technology (Tokyo Tech), Japan, in 1990, 1992, and 2000, respectively. From 1992 to 1995, he was with the Mechanical Engineering Research Laboratory, Hitachi Ltd. In 1995, he joined the Precision and Intelligence Laboratory (P&I Lab), Tokyo Tech, as a Research Associate, and became an Associate Professor and a Professor, in 2000 and 2010, respectively. He is currently a Professor with the Institute of Innovation Research (IIR), Tokyo Tech. His current research interests include micromechatronics and precision motion control.

• • •